Tel Aviv University

The Raymond and Beverly Sackler

Faculty of Exact Science

Parcellation of Brain Images using Shape analysis

Thesis submitted towards the M.Sc. Degree

of Tel Aviv University

School of Physics and Astronomy

Submitted by

Itay Fisher

This research work has been carried out under the supervision of

Prof. David Horn

and

Prof. Yaniv Assaf

September 2018

Table Of Content

Abstract

The cortical layers define the architecture of the gray matter and its neuroanatomical regions and are essential for brain function. They are often studied using T1 or T2 MRI analysis. Concentrating on the cortex it is of interest to present it as a parceled map of the structural MRI information, known as the parcellation of the brain.

We develop a novel methodology for investigating the 3d information of the MRI data. It is based on the recent finding that the Parzen probability distribution, which can be derived from such 3d imagery, can be decomposed into Weight and Shape components. Shape is independent of the bias field effect in MRI data; the latter is included in the Weight component.

We find that selecting a thresholded Shape component of T2 data, one obtains a good segmentation of the gray matter, without the need for any prior anatomical information. Confining ourselves to this data component, we perform clustering on it, and find the dominant closest clusters to the cortical surface, thus achieving parcellation of the brain. We demonstrate results of such analysis for four macaque brains and three rat brains.

For T1 analysis, the thresholded Shape component contains more than the gray matter information. Hence segmentation cannot be applied in the same manner as in T2 images. Nonetheless, parcellation can be derived by performing QC clustering of the full MRI image, followed by mapping onto the brain surface. This is demonstrated on three human brains. A comparison of the two parcellation methods for T2 data shows satisfactory agreement.

Our two methods are universal; i.e. they do not rely on expert anatomical knowledge, and they are applicable to all mammalian brains.

Chapter 1

1.1. Introduction

The task of understanding the structure of a brain and its effects on functionality and behavior has been a great challenge for over a century [1] and is still far from being accomplished. A major portion of research is based on variety of Magnetic Resonance Imaging (MRI) techniques [2] such as: Functional MRI, Diffusion MRI, MRN (Neurography) and more.

As the technologies of brain imaging evolve, so does the motivation and tools for brain mapping, leading to an increase in number and in quality of brain modeling and brain mapping collaborations and projects [3].

Brain segmentation methods, separation of brain MRI into different regions according to their physiological composition, differ by the techniques of image collection, regions of interest, and image processing methods. This enormous amount of variations leads to many different parcellation techniques, dividing the gray matter into separated regions of interest [4-6] and wide variety of brain atlases.

In this work we suggest a new multistage brain MRI image segmentation and parcellation method, based on the Quantum Clustering (QC) methodology [7]. The latter has recently been demonstrated to follow from the Shape component of data [8], building on its non-biased characteristics and edge sensitivity, features which are very useful for the analysis of the cortical mammal brain regions.

The method is applied to several kinds of mammalian brains (rats, macaques and humans are presented here) without invoking any prior customization. This separates our methodology from most other existing solutions.

We develop methods for both T1 and T2 weighting techniques. Method 1 allows for both segmentation of gray matter and brain parcellation in T2 images, and Method 2 provides parcellation for both T1 and T2 imaging.

1.2. Background

1.2.1. MRI:

Magnetic Resonance Imaging is a non-invasive scan, used for internal organs imaging. The scan is considered relatively safe and can be used as often as needed, because of the absence of ionizing radiation. The MRI mechanism relies on the magnetic resonance sensitivity of hydrogen, which is abundant in biological tissues.

In order to obtain an MRI image, a large constant magnetic field is applied to the hydrogen nuclei, which causes a perturbation to their protons' magnetic moments. While returning to their original states (relaxation phase) an electro-magnetic signal is emitted.

The emitted signal is than recorded for examination. The signal depends on three observed parameters:

a. Proton density
b. Spin-lattice relaxation time (T1)

by applying an RF Larmor frequency signal, one can flip the spins in opposite direction to the magnetic field. T1 describes the time to restore magnetization:

$$(1)\quad M_{||} = N\left[1 - e^{-\frac{t}{T_1}}\right]$$

where T1 has different values for different tissue types, N is the initial magnetization. This leads to contrast between CSF, fat and brain components as shown in figure 1c.

c. Spin-spin relaxation time (T2)

by using a weaker RF pulse and triggering a smaller flipped angle. The magnetization, parallel to the external magnetic field sums up to a smaller signal and the magnetization transverse to the original direction sums up to:

$$(2)\quad M_{T_{\perp}} = Ne^{-\frac{t}{T_2}}$$

a measurable signal. where T2 has different values for different tissue types, thus providing contrast between CSF, fat and brain components as shown in figure 1d.

The overall signal of the described spin echo mechanism obeys the following equation:

$$(3)\, signal = K[H]\frac{(sin\alpha)(1-e^{-\frac{TR}{T1}})}{1-(cos\alpha)e^{-TR/T1}}e^{-\frac{TE}{T2}}$$

Where k is a scaling factor, $[H]$ is spin density, α represents the flip angle, TR is the time between two successive excitations of the same slice (repetition time), TE is the time between the excitation pulse and the peak of the signal (echo time).

1.2.2. Contrast mechanisms:

By using short repetition time and echo time we achieve a T1 sequence which gives high signal for fat and lower signal for water, as demonstrated in figure 1a.

Using both long TE and TR achieves a T2 sequence which gives higher signal for water and lower signal for fat, as demonstrated in figure 1b.

When examining a complex biological tissue, it is important to have the ability to differentiate between different ingredients. This capability is the main key which allows us to differentiate between brain's gray matter and white mater.

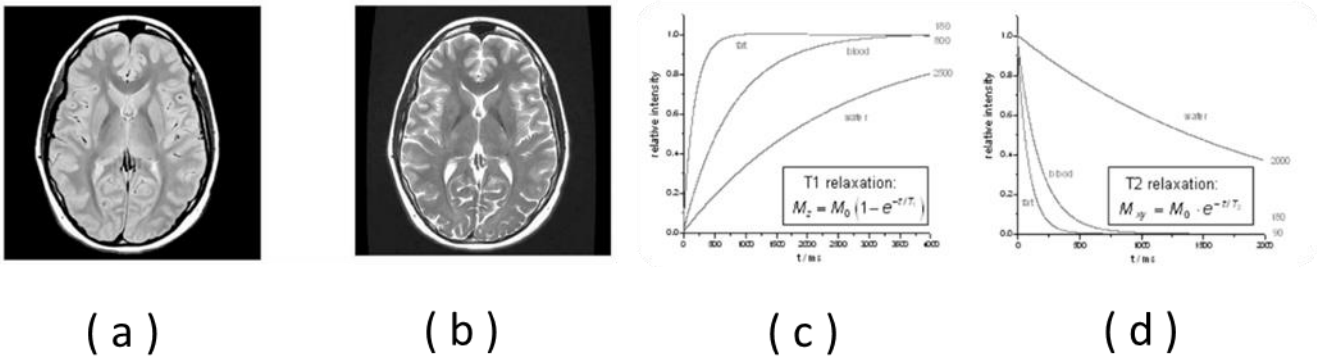

Figure 1. a. T1: Short TR Maximizes T1 contrast due to different degrees of saturation. Short TE Minimizes T2 influence, maximizes signal. b. T2: Long TR Minimizes influence of different T1 and Long TE Maximizes T2 contrast- Relatively poor SNR. c.T1

The following table summarizes the different matter characteristics, using different weighting techniques:

Tissue	T1 weighted	T2 weighted
CSF	Dark	Bright
White matter	Light	Dark gray
Cortex	Gray	Light gray
fat	Bright	light

1.2.3. Learning and Adaption

Any method that incorporates information from training samples in the design of a classifier employs learning. Creating classifiers involves positing some general model of the classifier and using training patterns to learn or estimate the unknown parameters of the model. Learning refers to some sort of algorithm for reducing the error on the net training data. There are three families of learning algorithms: supervised learning, non-supervised learning and reinforcement learning.

a. In supervised learning, a teacher provides a category label or cost for each pattern in a training set and seeks to reduce the sum of costs for these patterns.
b. In unsupervised learning or clustering there is no explicit teacher and the system forms clusters or "natural grouping" of the input patterns.
c. In reinforcement learning no desired category signal is given. Instead, the only teaching feedback is that the tentative category is right or wrong. The algorithm uses a known target category label to improve the classifier until a satisfying category is reached.

1.2.4. MRI segmentation

Image segmentation is commonly used for measuring and visualizing brain structures. The goal of image segmentation is to divide an image into a set of homogenous and nonoverlapping regions of similar attributes such as intensity, color or texture. In the case of brain MRI, image elements are typically classified into three main tissue types: white matter, gray matter, and cerebrospinal fluid (CSF).

There are five main families of methods which are used for brain MRI segmentation [9]:

1)Manual segmentation, where a human operator segments an image by hand

2) Intensity-based methods classify individual pixels/voxels based on their intensity [12].
3) Atlas based methods. The atlas contains information about the brain anatomy and it is used as a reference for segmenting new images.
4) Surface based methods, such as deformable models including active contours and surfaces. [13]
5) Hybrid segmentation methods, using a combination of several techniques to obtain the segmentation goal.

1.2.5. Brain parcellation

Brain parcellation means dividing the brain's surface into parcels which represent non-overlapping regions of homogeneity of the gray matter with respect to specific features, such as anatomical connectivity, functional connectivity and more.

Because of the need of learning and grouping the data into unified sets, brain parcellations are often derived from clustering algorithms applied to brain images [14].

There are three main techniques commonly used for brain parcellation: anatomical or functional ROI (regions of interest), brain atlas based and data driven parcellation.

a. Functional region of interest: brain parcellation consists of building a summary of signals in a predefined region. The method is limited to the scope of the specific region and ignores any peripheral signals; therefore, the method is extremely sensitive inside the region's boundary but may suffer from disability to fit the bigger picture. FROI analyses are particularly useful for investigating phenomena with distinctive, well-described, and anatomically restricted features [10], e.g. V1, MT, and the fusiform face area.
b. Atlas based parcellation is useful when dealing with wider areas of the brain, and even full brain analysis. The method involves a known prior parcellation of a well-defined atlas. The atlas can serve as a reference template for studies of functional data or neuroanatomy, or as a statistical prior for segmentation algorithms. The atlas can provide a basis for the analysis of automated image

segmentation methods, serving as training data for machine learning algorithms [11]

c. Data driven parcellation uses different algorithms in order to group voxels with similar attributes or functional activity together. The variety of different clustering techniques and their flexibility to seek after different features appears to be a very useful tool. [https://arxiv.org/pdf/1802.04353.pdf]

1.3. Thesis organization

The remainder of the thesis is organized as follows: in section 2, we present the methods tested in this study and the criteria for model evaluation.

In section 3 we describe our experiments on real data, illustrating the methodology in details for one test case: macaque #3. The rest of test cases and our model evaluation are presented in section 4.

Conclusions regarding the algorithms and the parcellation schemes are drawn in section 5.

Chapter 2

2. Methodology

Our study suggests a novel methodology for brain parcellation which may be used for different types of mammals: rat, macaques and human alike.

We use a data driven method in order to parcellate MRI images into different numbers of clusters, using the Quantum Clustering algorithm. We study its relevance by following the Weight-Shape decomposition procedure.

2.1. Weight-shape decomposition

Given an image defined by intensities I_i in discrete voxels **i** in a 3D Euclidean space, one defines its Parzen [17] (un-normalized) probability distribution by

$$P(\boldsymbol{x}) = \sum_i K(\boldsymbol{x} - \boldsymbol{x_i})\, I(\boldsymbol{x_i}) \quad (4)$$

where K is the Gaussian kernel: $K(\boldsymbol{z}) = exp\left(-\frac{\boldsymbol{z}^2}{2\sigma^2}\right)$, and $\boldsymbol{x_i}$ is the location of the image pixel.

Following [8] we employ the Weight Shape decomposition:

$$P(\boldsymbol{x}) = W(\boldsymbol{x})S(\boldsymbol{x}) \quad (5)$$

where

$$S(\boldsymbol{x}) = \exp\big(-V(\boldsymbol{x})\big) \quad (6)$$

The potential function, $V(\boldsymbol{x})$, is related to the Parzen probability P by the Schrodinger equation:

$$-\frac{\sigma^2}{2}\nabla^2 P(\boldsymbol{x}) + P(\boldsymbol{x})V(\boldsymbol{x}) = \frac{d}{2}P(\boldsymbol{x}) \quad (7)$$

Where d represents the Euclidean space dimension in which the data points reside.

Weight is related to an entropy function *H* by:

$$H(\boldsymbol{x}) = \log W(\boldsymbol{x}) = \mathrm{V}(\mathbf{x}) + log\mathrm{P}(\mathbf{x}). \quad (8)$$

This decomposition allows for three families of clustering algorithms [8], based on maximization of P, maximization of S, and maximization of H. The first method coincides with Mean-Shift [15], and the second coincides with Quantum Clustering (QC) [7] which is based on minimization of V.

On a finite lattice described by discrete voxels **i** one can rewrite the potential (up to a constant) in terms of convolutions

$$\boldsymbol{V}(\boldsymbol{x}) = \frac{\sum_{\mathbf{i}} \boldsymbol{L}(\boldsymbol{x}-\boldsymbol{x_i})\boldsymbol{I}(\boldsymbol{x_i})}{\sum_{\mathbf{i}} \boldsymbol{K}(\boldsymbol{x}-\boldsymbol{x_i})\boldsymbol{I}(\boldsymbol{x_i})} \quad (9)$$

where

$$\boldsymbol{L} = -\boldsymbol{K}\log\boldsymbol{K}. \tag{10}$$

and $\boldsymbol{L}$ is the discrete realization of the Laplace operator.

As a simple illustration, we plot in Fig. 2 the different shape functions for a two-dimensional star figure.

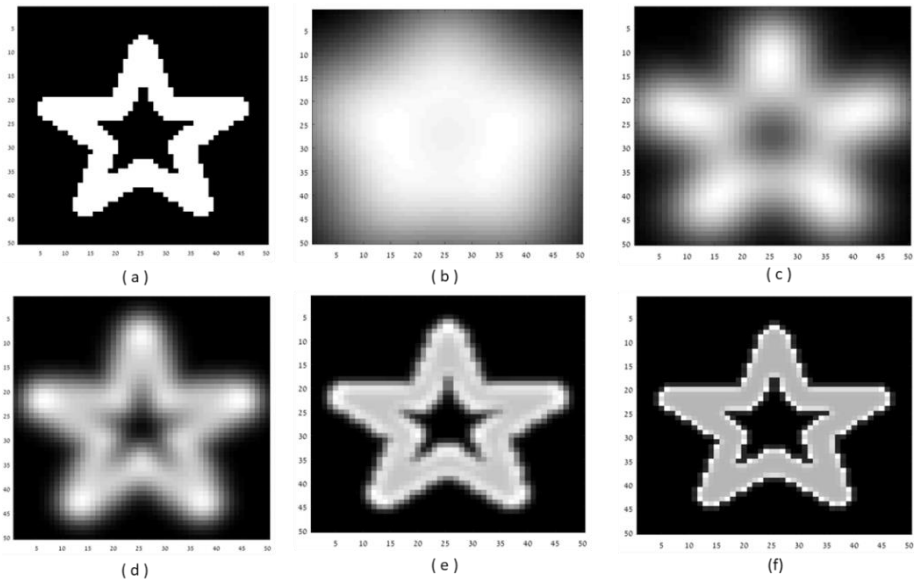

Figure 2. Shapes for different sizes of σ. (a) the original image. (b-f) shapes for $\sigma = 10, \sigma = 5, \sigma = 2.5, \sigma = 1, \sigma = 0.5$ accordingly. Note that the edges are much brighter than the rest of the image. We shall use this unique behavior for filtering data later on

The advantage of the weight-shape decomposition is that weight depends on the semi-local scale of *P*, whereas *V* is free of such bias. Hence *V* and *S* reflect local variations in *P*.

2.1.1. Bias field

Bias field signal is a low-frequency and very smooth signal that corrupts MRI images, especially those produced by old MRI machines [18]. Because of the bias inhomogeneity, it has a significant influence over both segmentation and parcellation algorithms that use grey level values of image pixels. Therefore, a pre-processing procedure is required in order to eliminate the described corruption.

A variety of different algorithms were developed for this purpose, using fuzzy *c*-means [18], intensity-based clustering [16], kernel-based clustering [19] and more.

We take advantage of the fact that when Shape is formed out of *P=WS*, non-local bias is eliminated through the fact that it belongs to Weight. This is demonstrated in Fig. 3.

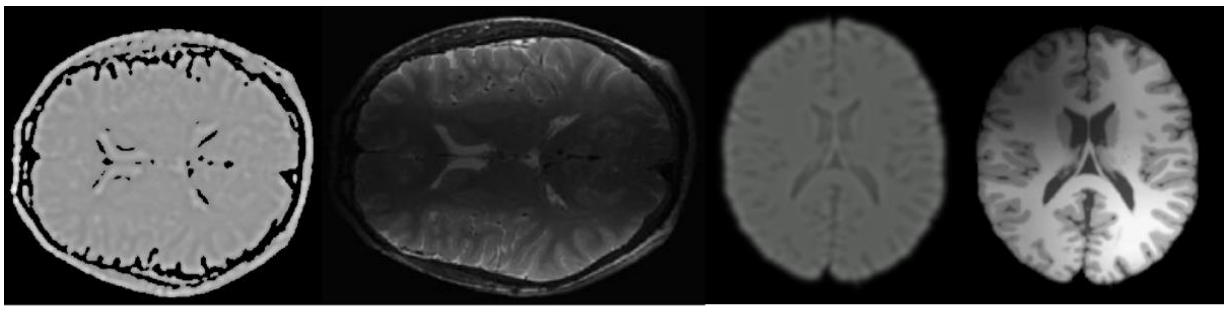

Figure 3. Example of bias field reduction by using weight shape decomposition. (a)T2 MRI brain shape. (b) biased T2 image (c) T1 MRI brain shape. (d) biased T1 MRI image. It is easy to notice that bias elimination is achieved by using our method, which derives (a) from (b) and (c) from (d).

2.1.2. Weight Supplementary Information

We define thresholded amplitudes, where we limit $\bar{W}$ by considering W values above the threshold W=0.6, and $\bar{S}$ by limiting S to contain values higher than S=0.25. This allows us to cover complementary regions in the brain, as exemplified in Fig. 4. Concentrating on the cortical regions we continue below with clustering of $\bar{S}$.

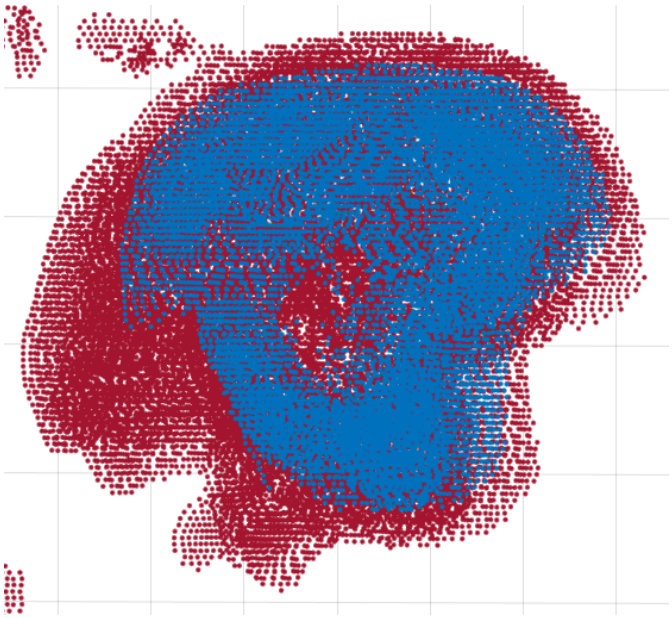

Figure 4. thresholded shape (red) and thresholded weight (blue) different dominant regions using the same MRI image. Data outside the brain are due to noise in the MR image.

2.2. Quantum Clustering

Clustering is performed using the QC method, which involves gradient descent of replica of data points to their nearest minimum of V. This method requires a choice of σ. The higher σ becomes, the larger the clusters will be, resulting correspondingly in overall smaller numbers of clusters.

This clustering procedure is illustrated in Fig.5, on a simple example of two dimensional datapoints.

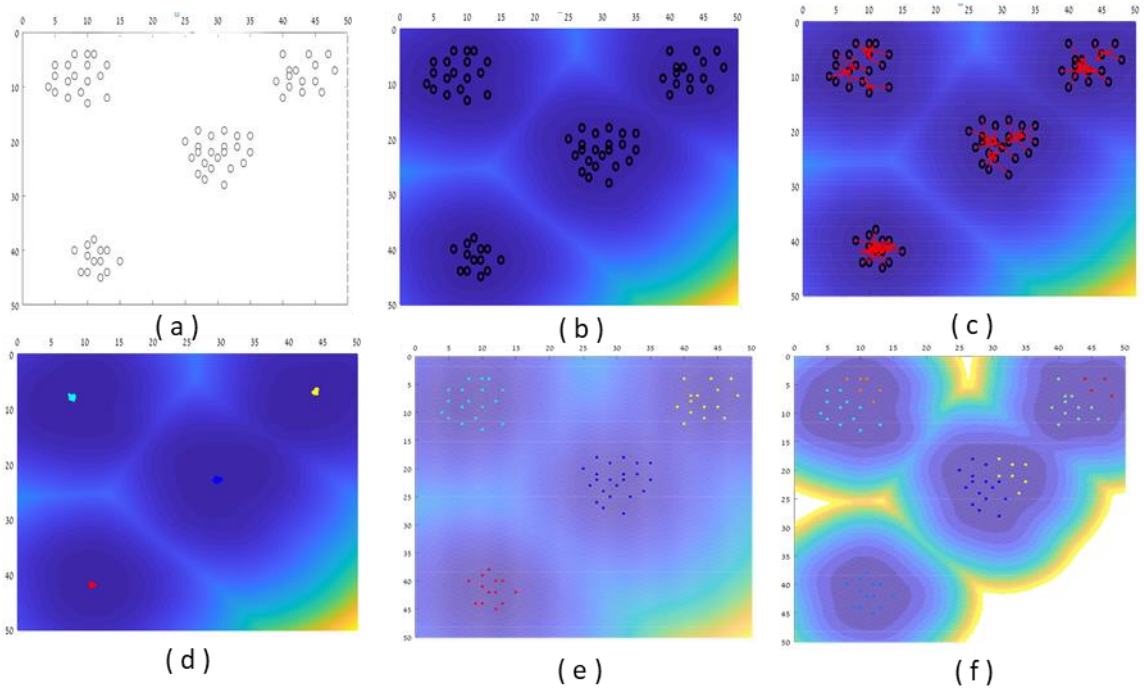

Figure 5 (a) illustrates synthetic data residing in a 50 by 50 pixels region. (b) illustrates the given points in the presence of the potential V, calculated for $\sigma = 3$, where dark blue represents low V values and yellow represents high values. (c) illustrates the procedure of gradient descent for the first step. (d) represent the last step (8 in this case) and the grouping by location. (e) shows the original data as clustered by QC. (f) displays the calculated potential and the corresponding clustering results for $\sigma = 2.5$.

Figures 5e and 5f demonstrate the importance of σ size and the need to determine its values to suit the data's typical dimensions or to the number of desired clusters.

2.3. The Brain Parcellation Algorithm

METHOD 1 (segmentation and parcellation for T2)

this multistep algorithm combines weight-shape decomposition and quantum clustering in order to segment the gray matter from a given MRI image and parcellate it into sub components:

a. Noise reduction.
b. Brain segmentation, using weight shape decomposition.
c. Quantum clustering of the gray matter.
d. Use the clusters for parcels classification.

METHOD 2 (parcellation only for both T1 and T2)

This simplified version skips over the segmentation step and employs QC over all brain data points.

Method 2 leads to a parcellation result which is similar to Method 1, as will be demonstrated in section 4 on a T2 image. It is applicable to both T1 and T2 MRI procedures. We applyy Method 2 to a human brain image in chapter 4.

a. Noise reduction

It is important to reduce the noise of the MR image. We do it by filtering out all I values which are smaller than 10% of the maximal I value. The importance of this procedure is exemplified in Fig. 6. If this noise is not filtered out the Shape acquires an unwarranted halo at the brain surface. Clearly the filtering does not affect the image while it clears the false background in the shape calculation.

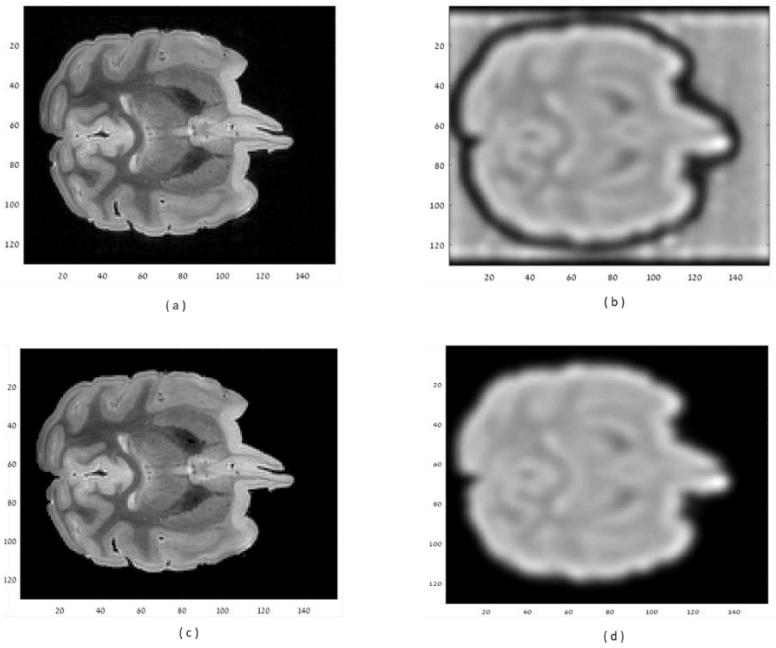

Figure 6 shape representation for filtered and non-filtered macaque #3 MRI brain image. (a) the original MRI image, layer z=70. (b) the corresponding calculated Shape for the original MRI image, layer z=70. (c) the filtered MRI image, layer z=70. (b) the corresponding calculated Shape for the filtered MRI image, layer z=70.

b. Shape calculation and gray matter segmentation

We shall calculate the shape for the filtered MRI images, using different σ sizes.

We define thresholded S by considering only contributions which have high values, higher than S=0.225. Let us denote the resulting distribution by $\overline{S}$. The latter is expressed mainly in the cortical regions dominated by gray matter, as seen in Fig. . This becomes our segmentation procedure.

c. Quantum Clustering

Quantum Clustering will be applied to I data restricted to the segmented area in Method 1, or to all noise-reduced data in Method 2, for different σ values (3,5,7 pixels). In order to reduce computational complexity, we pick randomly n=30,000 data points from the gray matter region.

Being interested in the strongest clusters, we order them by their strength, defined by $G_\alpha = \sum_{i\epsilon\alpha} I_i$,where α denote a cluster index and I_i represents the intensity of data-point i..

d. Cortex parcellation

An outer surface of all data points is constructed by a standard Matlab triangulation procedure *isosurface*. Each triangle on the resulting mesh of the cortical layer is attributed to a specific cluster, determined by the majority of the clusters met along five steps toward the center of the brain, with the direction orthogonal to the triangle.

Cortical datapoint parcellation

1. For each triangle of the mesh
2. Calculate its normal
3. Proceed 5 steps along the normal
4. At each step keep the identity of the nearest cluster met along the normal
5. end

2.4. Segmentation evaluation.

Comparison between different segmentation methods

Our shape-based segmentation will be compared to another segmentation algorithm by using the Jaccard index [20], calculating an appropriately normalized overlap between them.

$$\boldsymbol{J(A,B) = \frac{A \cap B}{A \cup B}}$$

The method to be compared with is the Multiplicative intrinsic component optimization (MICO) for MRI bias field estimation and tissue segmentation [16].

2.4.1.1. Parcellation evaluation.

Evaluation of the parcellation results is a challenge by itself. Observation of the results and comparing to familiar atlases may give us a feeling about its success, but a non-quantitative evaluation means nothing but a hunch.

We now introduce two main parameters to be quantitatively examined: stability and reproducibility.

2.4.1.2. Normalized Mutual Information

A well-known [21] method used to quantitatively evaluate the similarity between two clustering results is the Normalized Mutual Information (NMI) matrix:

$$M(A,B) = \frac{\sum_{i=1}^{N}\sum_{j=1}^{N} p(A_i,B_j)\log\left(\frac{p(A_i,B_j)}{p(A_i)p(B_j)}\right)}{\left(-\sum_{i=1}^{N} p(A_i)\log(p(A_i)) - \sum_{i=1}^{N} p(B_i)\log(p(B_i))\right)/2} \quad (11)$$

$$where$$

$$p(A_i) = \frac{size(A_i)}{\sum_{j=1}^{N} size(A_j)}; p(A_iB_i) = \frac{size(A_i \cap B_j)}{\sum_{i=1}^{N} size(A_i)} \quad (12)$$

The measure M falls in the range of 0 to 1 where 0 means that the clustering methods are completely dissimilar to each other, and 1 means full similarity.

We shall use this parameter for evaluating the algorithm's stability and reproducibility, where we define

Stability= small change in M as $\boldsymbol{\sigma}$ varies for the same MRI image.

Reproducibility= small change in M for different registered MRI images and the same $\boldsymbol{\sigma}$ value.

Since two meshes usually don't fit exactly each other, we calculate the NMI according to the triangles that do fit. We denote the fraction of consistent triangles by r. For example: if one parcellation has 100 classified triangles and the other has 200 classified triangles, we look for the triangles which suit both parcellations. If they sum up to 80 than $r = \frac{80}{100} = 0.8$.

Chapter 3

3. Test cases

We analyze three types of mammalian brains: rats, macaques and humans. The mammalian brains differ from each other by their size, shape and structure as shall be demonstrated later on.

For macaque #3 we present the entire algorithm explicitly for different sizes of $\boldsymbol{\sigma}$ in order to illustrate its significance. This will also enable us to evaluate the suited $\boldsymbol{\sigma}$ for each test case.

We present a short description of the rest of the test cases in order to evaluate the algorithm stability and reproducibility.

3.1. Data

We use different mammalian brains in order to demonstrate our parcellation algorithm. They are summarized in the next Table.

test case	name	Size [pixels]	Type	Weight	Source	Intensity scale
1	Macaque #3	130X156X130	Macaque	T2	TAU	0-1
2	Macaque #5	130X156X130	Macaque	T2	TAU	0-1
3	Macaque #7	130X156X130	Macaque	T2	TAU	0-1
4	Macaque #9	130X156X130	Macaque	T2	TAU	0-1
5	Wild rat	130X156X130	Rat	T2	TAU	0-1
6	Rat #1	130X156X130	Rat	T2	TAU	0-1
7	Rat #6	130X156X130	Rat	T2	TAU	0-1
8	MaNa	130X156X130	Human	T1	TAU	0-1
9	KaYo	130X156X130	Human	T1	TAU	0-1

3.1.1.Macaque #3- detailed illustration

We use a T2 MRI notation, where higher intensity values represent gray matter, while lower intensity values represent white matter.

Segmentation:

the following figure displays the shape weight decomposition and its resulting segmentation for $\sigma = 3$:

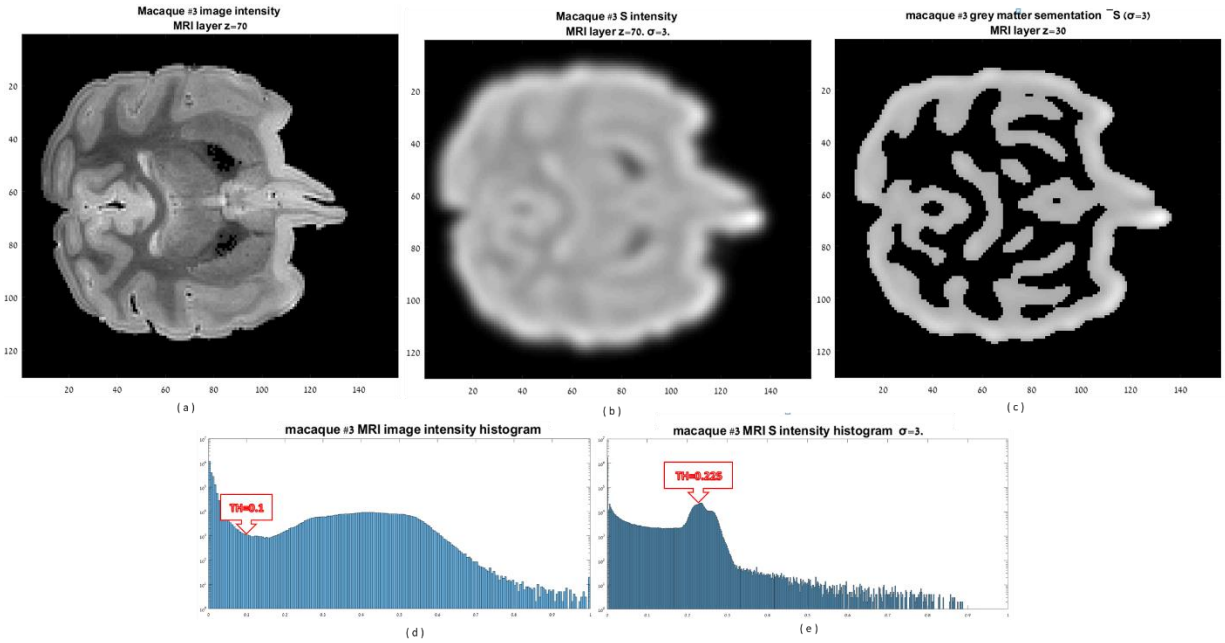

Figure 7. macaque #3 segmentation evaluation using Shape methodology,$\sigma = 3$.(a) the MRI image for layer z=70, after noise reduction. (b) the corresponding shape, for $\sigma = 3$.(c) the grey matter segment , ilustrated by $\overline{S}$.(d) total MRI histogram and the threshold used for noise reduction.(e) macaque #3 shape histogram, and the threshold used for $\overline{S}$ definition.

By the same method we segmented the gray matter for $\sigma = 5, 7$ and 9:

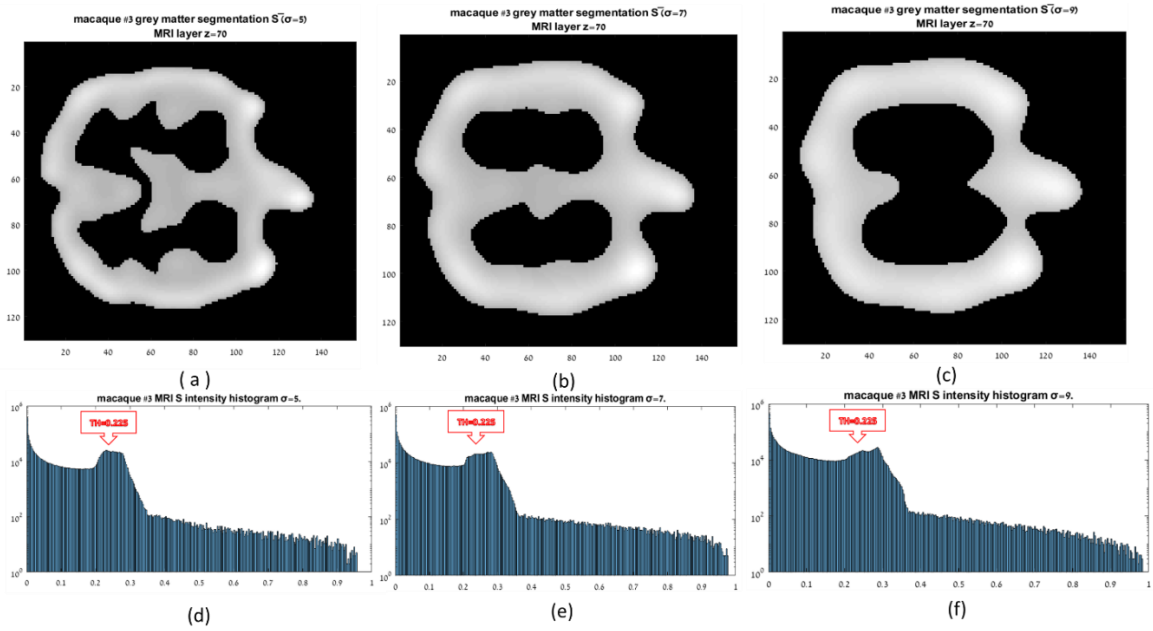

Figure 8. macaque #3 segmentation using the Shape methodology for different σ .sizes (a) σ=5. (b) σ=7.(c) σ=9.(d) shape intensity histogram for σ=5.(e)shape intensity histogram for σ=7.(f) shape intensity histogram for σ=9

An alternative segmentaion method, Multiplicative Intrinsic Component Optimization (MICO) for MRI bias field estimation and tissue segmentation [16], leads to the result displayed in Fig. 9 for the same z=70 layer. We will compare the two methods in section 4, using the Jaccard coefficient.

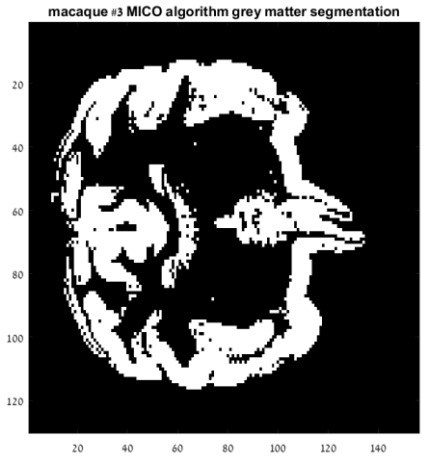

Figure9. MICO grey matter segmentation

Quantum Clustering results:

After apllying QC to the segmented region, we obtained the following results for different σ values in Figures 10 to 12. Subfigures a-f display sifferent steps of the QC algorithm. Colors are defined according to the final clusters (f). Subfigures g-i represent clustering results on three perpendicular planes. $\sigma = 3$:

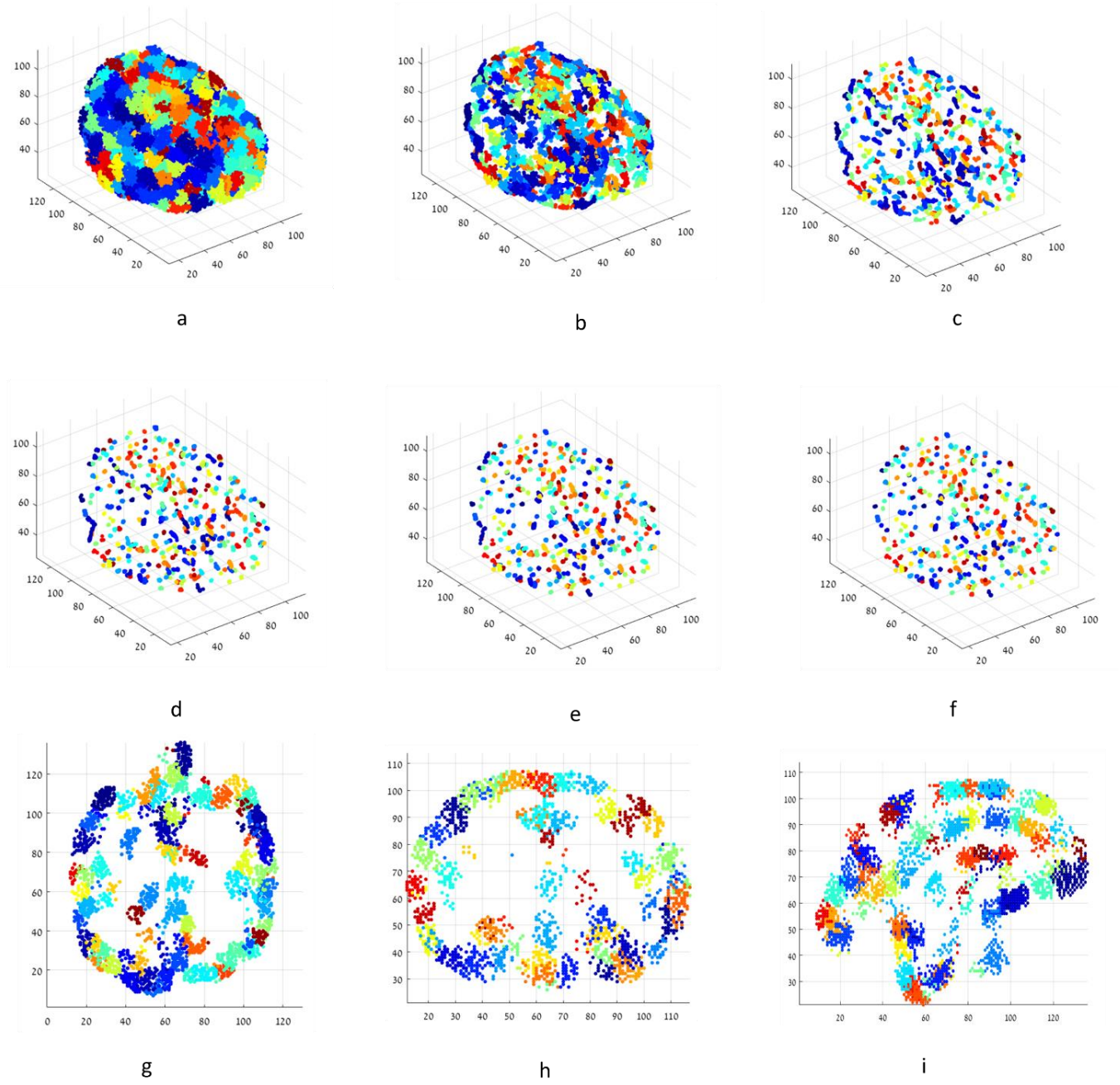

*Figure 10.brain datapoints clustering, using quantum clustering method **σ=3**. (a) initial position. (b) position after 5 iterations. (c) position after 10 iterations. (d) position after 20 iterations. (f) position after 50 iterations (g) the original data points divided into clusters-X_Y plane .(h) the original data points divided into clusters-Z_X plane.(i) the original data points divided into clusters-Y_Z plane.*

$\sigma = 5$

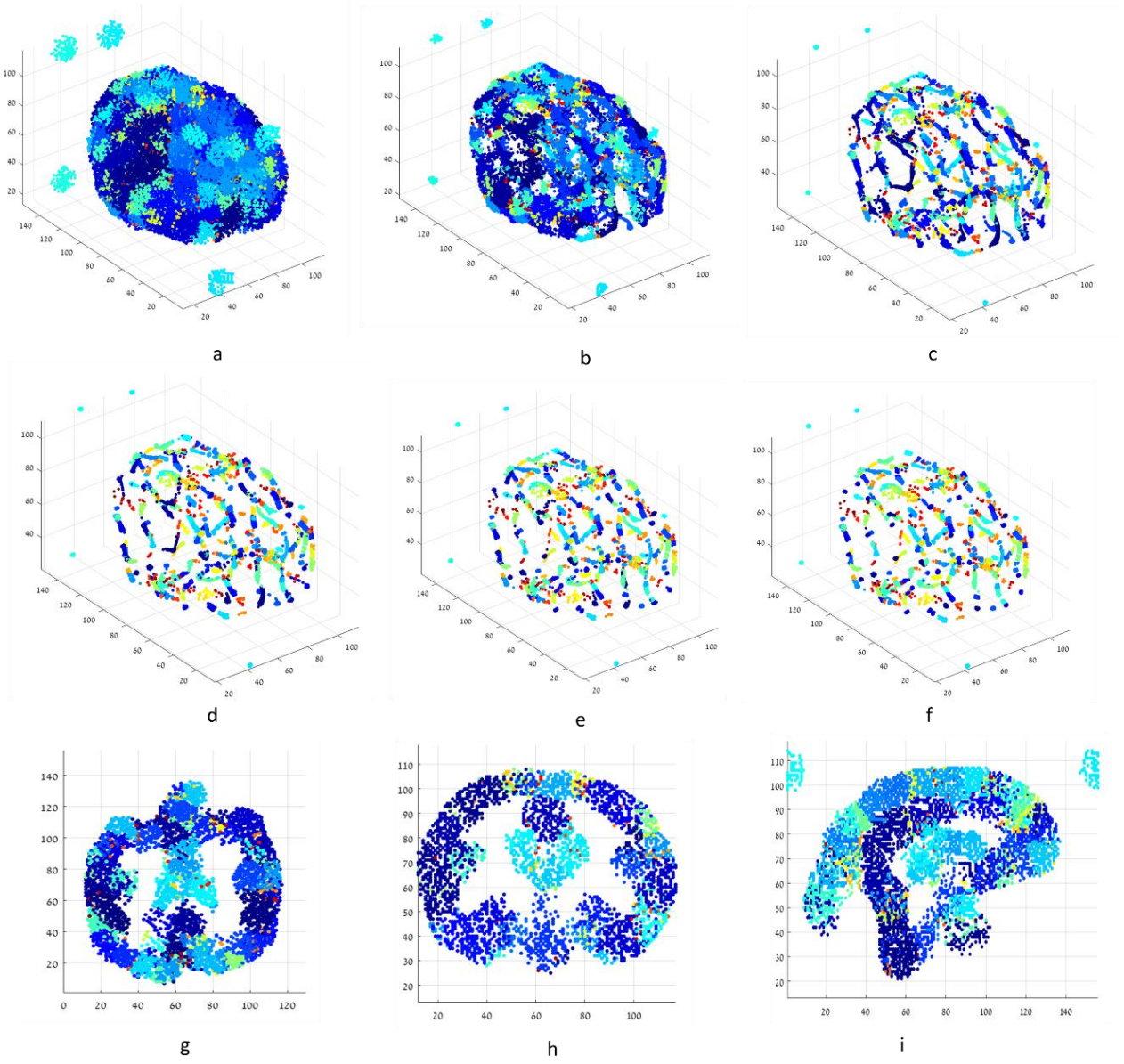

*Figure 11.brain datapoints clustering, using quantum clustering method **σ=5**. (a) initial position. (b) position after 5 iterations. (c) position after 10 iterations. (d) position after 20 iterations. (f) position after 50 iterations (g) the original data points divided into clusters-X_Y plane .(h) the original data points divided into clusters-Z_X plane.(i) the original data points divided into clusters-Y_Z plane.*

$\sigma = 7$

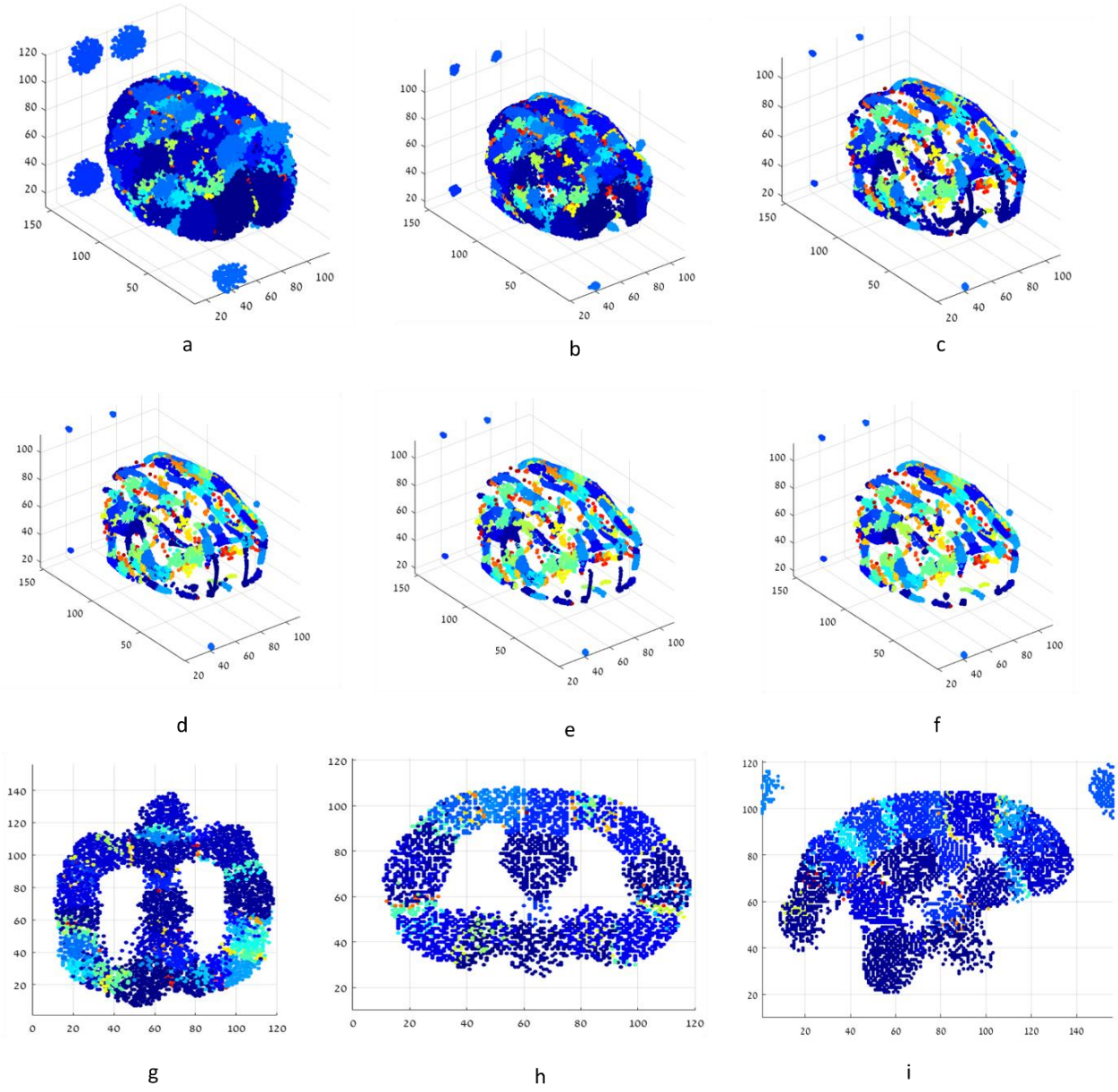

*Figure 12.brain datapoints clustering, using quantum clustering method **σ=7**. (a) initial position. (b) position after 5 iterations. (c) position after 10 iterations. (d) position after 20 iterations. (f) position after 50 iterations (g) the original data points divided into clusters-X_Y plane. (h) the original data points divided into clusters-Z_X plane. (i) the original data points divided into clusters-Y_Z plane.*

Final parcellation:

σ = 3

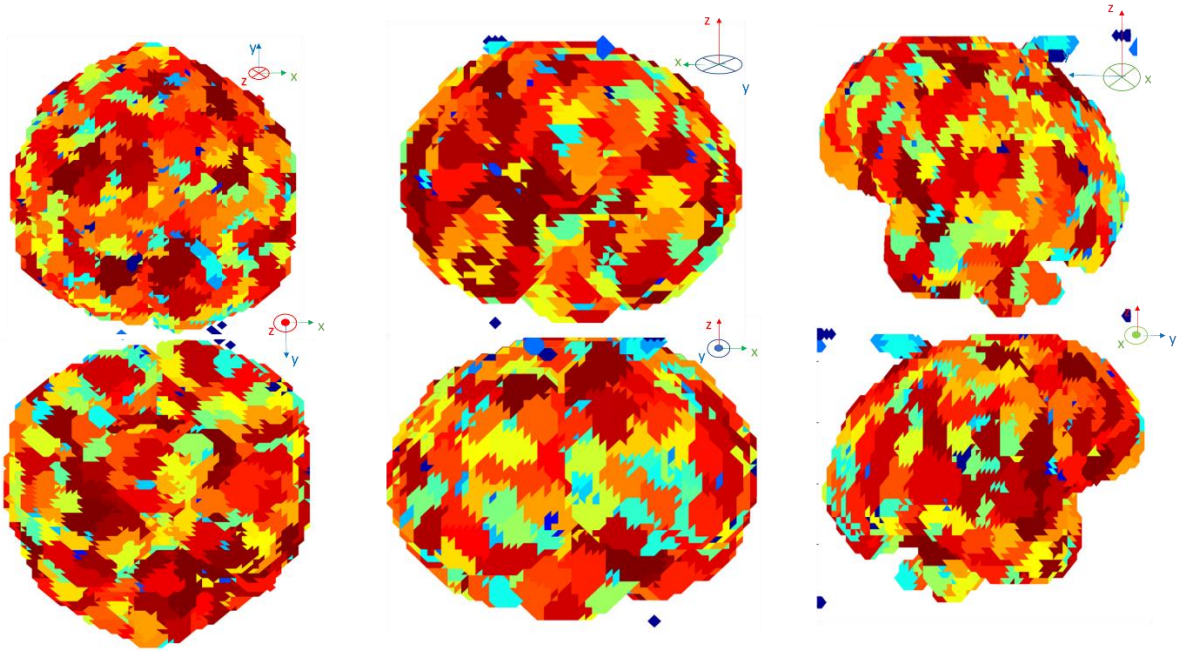

σ = 5

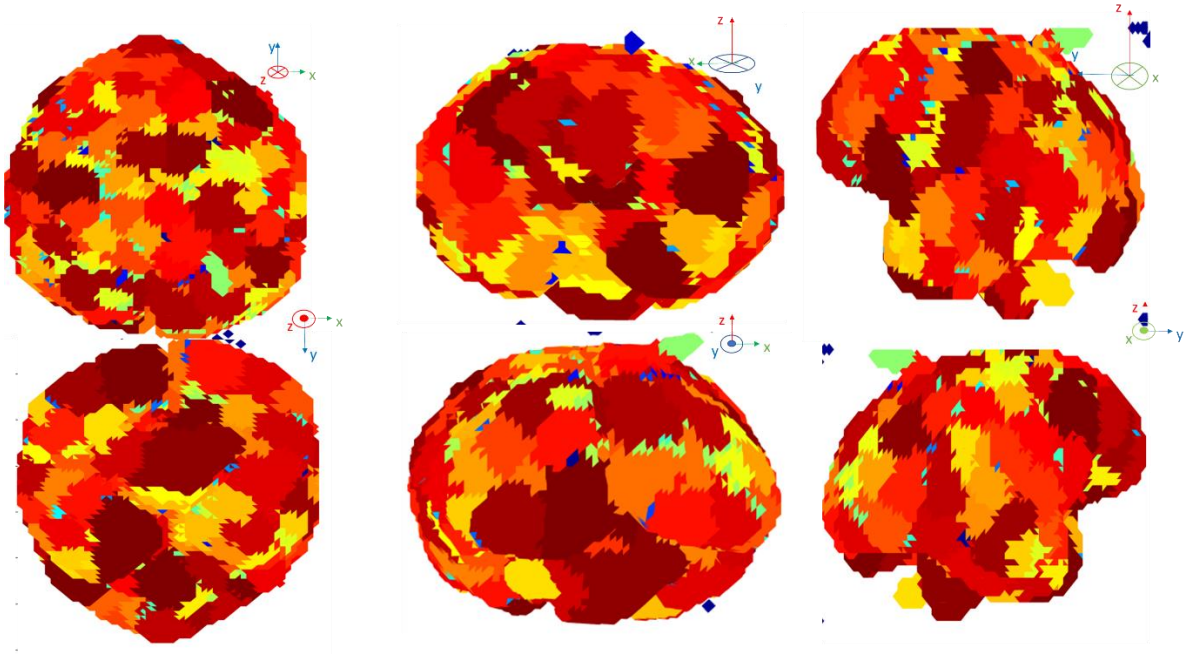

$\sigma = 7$

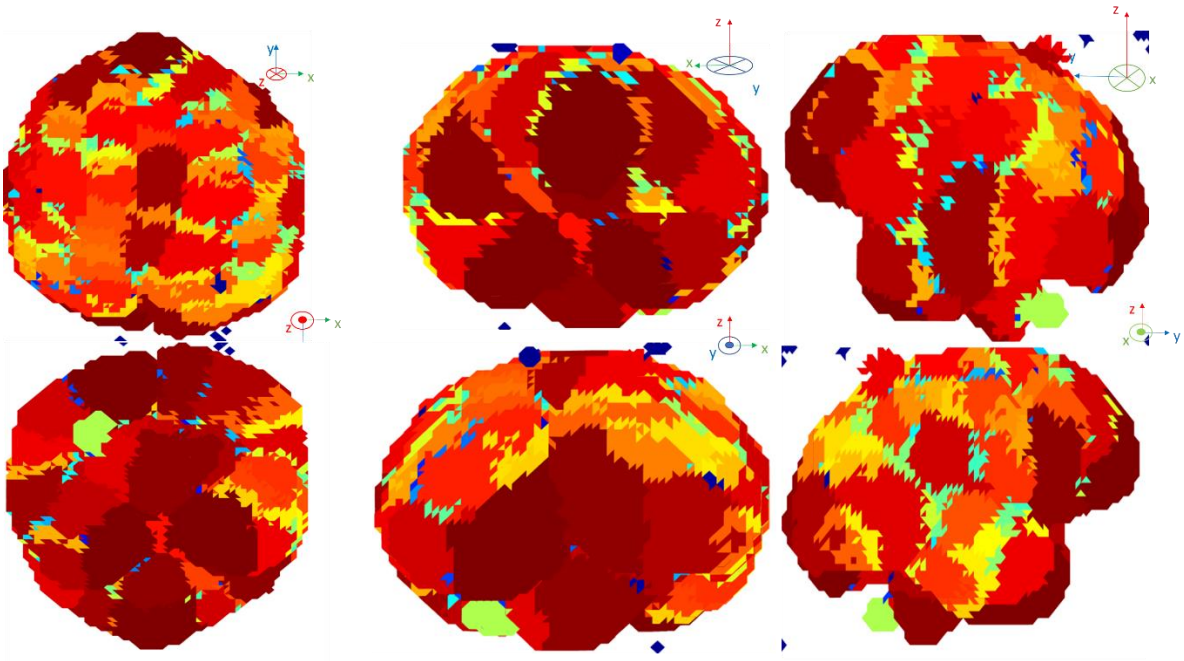

It is easy to notice that for increasing sizes of $\boldsymbol{\sigma}$, cluster sizes increase and the number of different parcels decreases.

This interesting connection motivated us to seek a suitable $\boldsymbol{\sigma}$ for each of the mammalian brain types. We simulated the entire algorithm for $\boldsymbol{\sigma}$ in the range of [3,9] in 0.2 resolution. The following graph illustrates the relationship between $\boldsymbol{\sigma}$ and the resulting number of parcels.

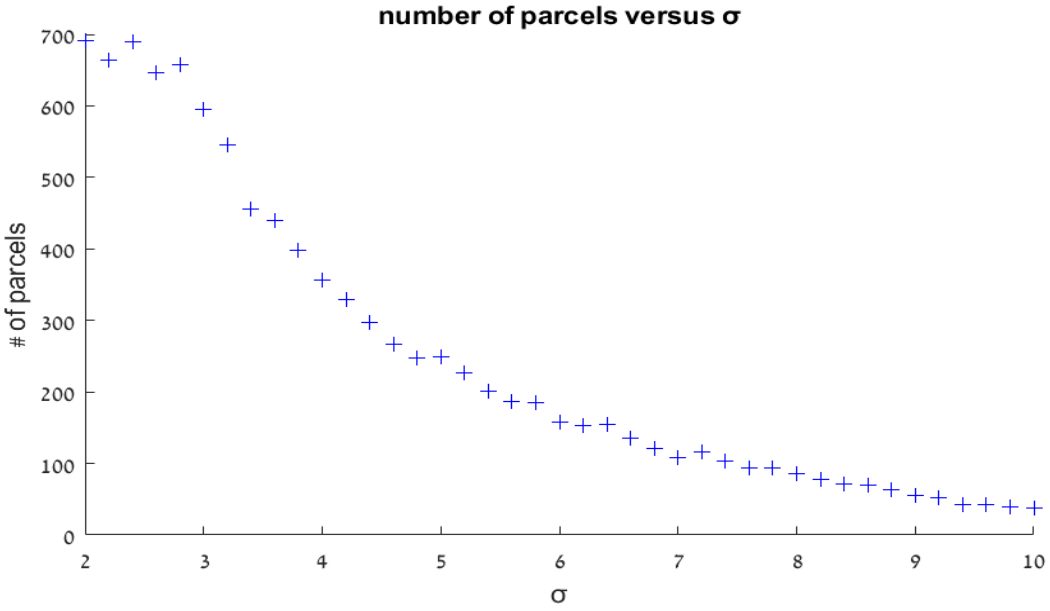

Figure13. number of different parcells versus $\boldsymbol{\sigma}$ size

Chapter 4

4. Results

4.1. Macaques

4.1.1. Summary of our results- macaques:

name	σ	#data points	#clusters	#parcels	#triangles
Macaque #3	3	29244	1015	549	17188
	5	29883	421	261	
	7	29811	246	197	
Macaque #5	3	29758	1207	668	19655
	5	30017	478	283	
	7	30388	240	180	
Macaque #7	3	30746	1225	610	18101
	5	29847	498	262	
	7	30663	286	166	

4.1.2. *Segmentation* comparison to MICO's:

Jaccard index	$\boldsymbol{\sigma = 3}$	$\boldsymbol{\sigma = 5}$	$\boldsymbol{\sigma = 7}$
Macaque #3	*0.72*	*0.63*	*0.57*
Macaque #5	*0.61*	*0.54*	*0.5*
Macaque #7	*0.73*	*0.65*	*0.59*
Macaque #9	*0.7*	*0.61*	*0.54*

4.1.3. Stability

Macaque #3-MNI	$\boldsymbol{\sigma = 3}$	$\boldsymbol{\sigma = 5}$	$\boldsymbol{\sigma = 7}$
$\boldsymbol{\sigma = 3}$	*1* , $r = \mathbf{1}$	*0.77,* $r = 0.98$	*0.73,* $r = 0.97$
$\boldsymbol{\sigma = 5}$	*0.77,* $r = 0.98$	*1,* $r = \mathbf{1}$	*0.75,* $r = 0.97$
$\boldsymbol{\sigma = 7}$	*0.73,* $r = 0.97$	*0.75,* $r = 0.97$	*1* , $r = 1$

Macaque #5-MNI	$\boldsymbol{\sigma = 3}$	$\boldsymbol{\sigma = 5}$	$\boldsymbol{\sigma = 7}$
$\boldsymbol{\sigma = 3}$	*1* , $r = 1$	*0.77,* $r = 0.98$	*0.73,* $r = 0.97$
$\boldsymbol{\sigma = 5}$	*0.77,* $r = 0.98$	*1* , $r = 1$	*0.75,* $r = 0.97$
$\boldsymbol{\sigma = 7}$	*0.73,* $r = 0.97$	*0.75,* $r = 0.97$	*1* , $r = 1$

Macaque #7-MNI	$\boldsymbol{\sigma = 3}$	$\boldsymbol{\sigma = 5}$	$\boldsymbol{\sigma = 7}$
$\boldsymbol{\sigma = 3}$	*1* , $r = 1$	*0.77,* $r = 1$	*0.72,* $r = 0.98$
$\boldsymbol{\sigma = 5}$	*0.77,* $r = 1$	*1* , $r = 1$	*0.75* , $r = 0.98$
$\boldsymbol{\sigma = 7}$	*0.72,* $r = 0.98$	*0.75,* $r = 0.98$	1 , r = 1

4.1.4. reproducibility

$\boldsymbol{\sigma = 3}$-*NMI*	*Macaque #3*	*Macaque #5*	*Macaque #7*
Macaque #3	*1* , $r = 1$	*0.8,* $r = 0.5$	*0.8,* $r = 0.38$
Macaque #5	*0.8,* $r = 0.5$	*1* , $r = 1$	*0.8, r=0.72*
Macaque #7	*0.8,* $r = 0.38$	*0.8, r=0.72*	*1* , $r = 1$

$\boldsymbol{\sigma = 5}$-*NMi*	*Macaque #3*	*Macaque #5*	*Macaque #7*
Macaque #3	*1* , $r = 1$	*0.76,* $r = 0.49$	*0.76,* $r = 0.38$
Macaque #5	*0.76,* $r = 0.49$	*1* , $r = 1$	*0.76, r=0.71*
Macaque #7	*0.76,* $r = 0.38$	*0.76, r=0.71*	*1* , $r = 1$

$\boldsymbol{\sigma = 7}$-*NMI*	*Macaque #3*	*Macaque #5*	*Macaque #7*
Macaque #3	*1* , $r = 1$	*0.74, r=0.49*	*0.74,* $r = 0.38$
Macaque #5	*0.74, r=0.49*	*1* , $r = 1$	*0.73, r=0.71*
Macaque #7	*0.74,* $r = 0.38$	*0.73, r=0.71*	*1* , $r = 1$

4.2. Rats:

the following figure displays the shape-based segmentation for different σ for the wild rat:

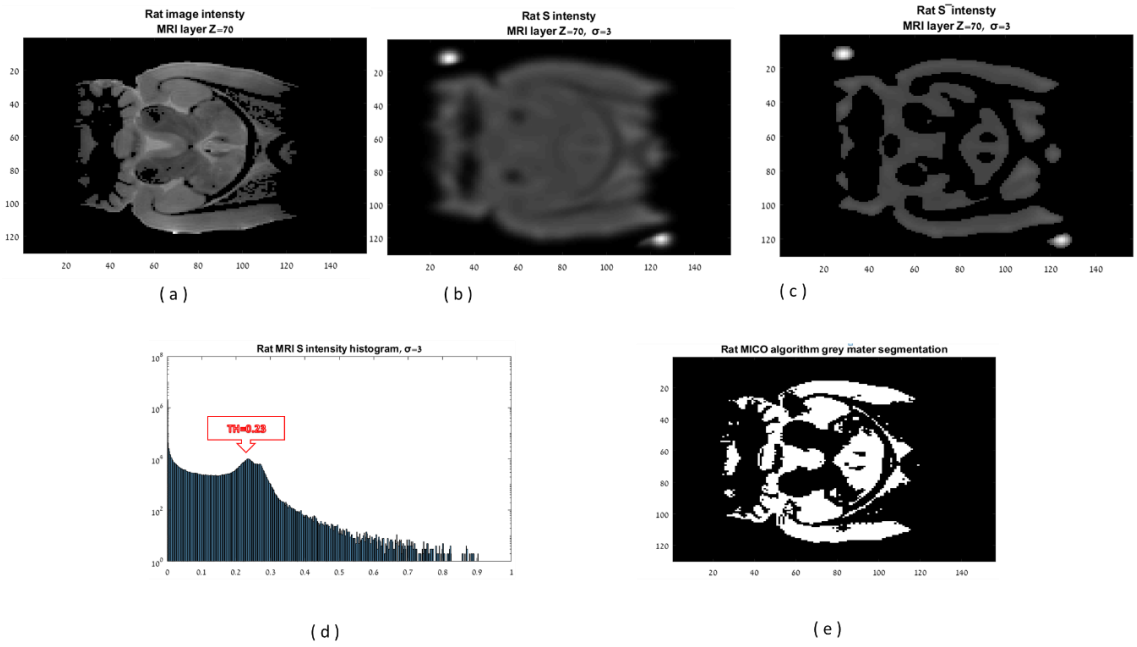

Figure 14.segmentation procedure for Wild Rat, using $\boldsymbol{\sigma} = \mathbf{3}$.(a) the MRI data- layer z=70.(b) shape distribution z=70, (c) thresholded s,(d) S intensity histogram.(e) MICO algorithm segmentation

Following clustering of the segmented region we obtained parcellations for "Wild Rat":

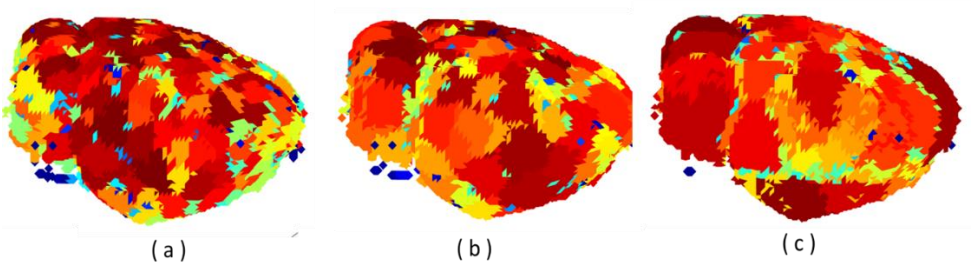

Figure 15. WIld Rat parcellation using different $\boldsymbol{\sigma}$ values.(a)$\boldsymbol{\sigma} = \mathbf{3}$,(b)$\boldsymbol{\sigma} = \mathbf{5}$,(c)$\boldsymbol{\sigma} = \mathbf{7}$

Summary of our results- rats:

name	σ	#data points	#clusters	#parcels	#triangles
Wild rat	3	30379	1074	675	24314
	5	28948	404	286	
	7	30266	217	171	
Rat #1	3	31035	1109	740	29385
	5	30623	450	307	
	7	30201	228	196	
Rat #6	3	29282	892	612	21826
	5	31625	338	258	
	7	31340	140	118	

4.2.1. Segmentation comparison to MICO's:

Jaccard index	$\boldsymbol{\sigma = 3}$	$\boldsymbol{\sigma = 5}$	$\boldsymbol{\sigma = 7}$
Wild rat	*0.64*	*0.63*	*0.6*
Rat #1	*0.6*	*0.55*	*0.52*
Rat #6	*0.49*	*0.43*	*0.39*

4.2.2. Stability

Wild rat	$\boldsymbol{\sigma = 3}$	$\boldsymbol{\sigma = 5}$	$\boldsymbol{\sigma = 7}$
$\boldsymbol{\sigma = 3}$	$1, \boldsymbol{r} = 1$	$0.75, r = 0.95$	$0.67, r = 0.92$
$\boldsymbol{\sigma = 5}$	$0.75, r = 0.95$	$1, r = 1$	$0.71, r = 0.91$
$\boldsymbol{\sigma = 7}$	$0.67, r = 0.92$	$0.71, r = 0.91$	$1, \boldsymbol{r} = 1$

Rat #1	$\boldsymbol{\sigma = 3}$	$\boldsymbol{\sigma = 5}$	$\boldsymbol{\sigma = 7}$
$\boldsymbol{\sigma = 3}$	$1, r = 1$	$0.75, r = 0.96$	$0.69, r = 0.91$
$\boldsymbol{\sigma = 5}$	$0.75, r = 0.96$	$1, r = 1$	$0.73, r = 0.91$
$\boldsymbol{\sigma = 7}$	$0.69, r = 0.91$	$0.73, r = 0.91$	$1, r = 1$

Rat #6	$\boldsymbol{\sigma = 3}$	$\boldsymbol{\sigma = 5}$	$\boldsymbol{\sigma = 7}$
$\boldsymbol{\sigma = 3}$	$1, \boldsymbol{r} = 1$	$0.73, r = 0.98$	$0.63, r = 0.95$
$\boldsymbol{\sigma = 5}$	$0.73, r = 0.98$	$1, r = 1$	$0.7, r = 0.95$
$\boldsymbol{\sigma = 7}$	$0.63, r = 0.95$	$0.7, r = 0.95$	$1, r = 1$

4.2.3. reproducibility

$\boldsymbol{\sigma = 3}$	*Wild rat*	*Rat #1*	*Rat #6*
Wild rat	$1, \boldsymbol{r} = 1$	$0.77, r = 0.61$	$0.77, r = 0.49$

Rat #1	$0.77, r = 0.61$	$1, \boldsymbol{r} = 1$	$0.77, r = 0.59$
Rat #6	$0.77, r = 0.49$	$0.77, r = 0.59$	$1, r = 1$

$\boldsymbol{\sigma = 5}$	*Wild rat*	*Rat #1*	*Rat #6*
Wild rat	$1, \boldsymbol{r} = 1$	$0.73, r = 0.57$	$0.73, r = 0.47$
Rat #1	$0.73, r = 0.57$	$1, r = 1$	$0.73, r = 0.57$
Rat #6	$0.73, r = 0.47$	$0.73, r = 0.57$	$1, r = 1$

$\boldsymbol{\sigma = 7}$	*Wild rat*	*Rat #1*	*Rat #6*
Wild rat	$1, \boldsymbol{r} = 1$	$0.71, r = 0.54$	$0.68, r = 0.45$
Rat #1	$0.71, r = 0.54$	$1, r = 1$	$0.67, r = 0.55$
Rat #6	$0.68, r = 0.45$	$0.67, r = 0.55$	$1, \boldsymbol{r} = 1$

4.3. Comparison of Method 2 and Method 1 parcellations:

4.3.1. Summary of Macaque #3 results using method 2:

name	$\boldsymbol{\sigma}$	#data points	#clusters	#parcels	#triangles
Macaque #3	3	30458	1257	576	17188
	5	30458	376	229	
	7	30458	214	153	

4.3.2. Comparison between method 1 and method 2 for macaque #3

Macaque #3	$\boldsymbol{\sigma = 3}$, *method 1*	$\boldsymbol{\sigma = 5}$, *method 1*	$\boldsymbol{\sigma = 7}$, *method 1*
$\boldsymbol{\sigma = 3}$, *method 2*	$0.82, r = 1$	$0.78, r = 0.98$	$0.73, r = 0.97$
$\boldsymbol{\sigma = 5}$, *method 2*	$0.77, r = \mathbf{1}$	$0.78, r = 0.98$	$0.75, r = 0.97$
$\boldsymbol{\sigma = 7}$, *method 2*	$0.69, r = 1$	$0.73, r = 0.98$	$0.74, r = 0.97$

The comparison between method 1 and method 2 shows consistency between the two methods. Hence we may continue and use method 2 for analysis of human brains.

4.4. Human brains

4.4.1. Summary of our results- humans:

name	σ	#data points	#clusters	#parcels	#triangles
KaYo	3	30273	1178	486	16534
	5	30273	367	209	
	7	30273	203	135	
MaNa	3	30382	1363	553	18216
	5	30382	396	234	
	7	30382	235	164	

4.4.2. Parcellation

Using QC clustering over the entire brain (Method 2) we obtained the following parcellations for "MaNa":

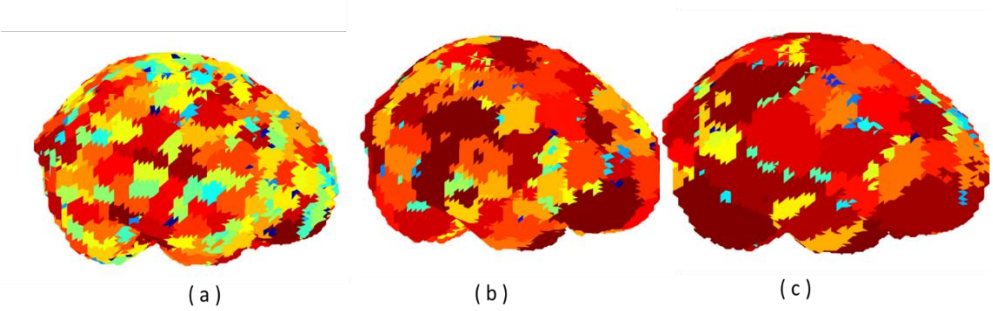

Figure 16. Human parcelation using different σ values.(a)σ=3,(b)σ=5,(c)σ=7

4.4.3. Stability

KaYo	$\boldsymbol{\sigma = 3}$	$\boldsymbol{\sigma = 5}$	$\boldsymbol{\sigma = 7}$
$\boldsymbol{\sigma = 3}$	$1, r = 1$	$0.81, r = 1$	$0.74, r = 1$
$\boldsymbol{\sigma = 5}$	$0.81, r = 1$	$1, r = 1$	$0.81, r = 1$
$\boldsymbol{\sigma = 7}$	$0.74, r = 1$	$0.81, r = 1$	$1, r = 1$

MaNa	$\boldsymbol{\sigma = 3}$	$\boldsymbol{\sigma = 5}$	$\boldsymbol{\sigma = 7}$
$\boldsymbol{\sigma = 3}$	$1, r = 1$	$0.8, r = 1$	$0.74, r = 1$
$\boldsymbol{\sigma = 5}$	$0.8, r = 1$	$1, r = 1$	$0.81, r = 1$
$\boldsymbol{\sigma = 7}$	$0.74, r = 1$	$0.81, r = 1$	$1, r = 1$

4.4.4. reproducibility

$\boldsymbol{\sigma} = \mathbf{3}$-*NMI*	*KaYo*	*MaNa*
KaYo	*1* , $r = 1$	*0.79* , r =*0.82*
MaNa	*0.79* , r =*0.82*	*1* , $r = 1$

$\boldsymbol{\sigma} = \mathbf{5}$-*NMI*	*KaYo*	*MaNa*
KaYo	*1* , $r = 1$	*0.76* , r =*0.82*
MaNa	*0.76* , r =*0.82*	*1* , $r = 1$

$\boldsymbol{\sigma} = \mathbf{7}$-*NMI*	*KaYo*	*MaNa*
KaYo	*1* , $r = 1$	*0.74*, $r = 0.82$
MaNa	*0.74*, $r = 0.82$	*1* , $r = 1$

Chapter 5

Summary and conclusions

The weight-shape formalism relates the quantum potential of a unique data-set with its equivalent energy. By using this formalism, combined with Quantum Clustering we have created a novel method for brain parcellation.

The method is unique in the sense of its universality to all kinds of mammals and its stability over a large range of parcel numbers, determined by the chosen scale σ .

As demonstrated for macaques, rats and humans, the method leads to stable outputs, examined by comparing parcellations for different σ sizes. It is shown that as σ is increased, the comparison value (NMI) with low σ decreases.

Reusability of the algorithm was examined by comparing different data sets of the same mammal and using the same σ scale satisfying pretty stable NMI values for each of the examined σ sizes. Most NMI values were around 0.75 which demonstrates a high consistency of the results.

Another unique achievement is the ability to cope with both T1 and T2 MRI imaging methods, with quite consistent results as examined for Rat datasets. Since T1 requires a whole brain clustering and T2 requires only the gray matter segmented areas, it is satisfying to witness NMI results reaching 0.82, showing consistency between the two parcellation methods.

The methods can be applicable to brain research, but may require further improvements, such as optimization of the ratio between σ and the specific MRI image resolution, and judicious selection of data points and software befitting constraints of computational complexity.

The code used for this work, and datasets studied here, are available at https://github.com/itayfisher/brain .

REFERENCES

[1] The human connectome: a complex network, Olaf Sporns, 04 January 2011

[2] Basic concepts of advanced MRI techniques, Pagani, E., Bizzi, A., Di Salle, F. et al. Neurol Sci (2008) 29(Suppl 3): 290.

[3] Human brain atlasing: past, present and future, Wieslaw L Nowinski , The Neuroradiology Journal 2017

[4] Alexander Schaefer, Ru Kong, Evan M. Gordon, Timothy O. Laumann, Xi-Nian Zuo, Avram J. Holmes, Simon B. Eickhoff, B.T. Thomas Yeo; Local-Global Parcellation of the Human Cerebral Cortex from Intrinsic Functional Connectivity MRI, Cerebral Cortex , https://doi.org/10.1093/cercor/bhx179 , *Cerebral Cortex*, Volume 28, Issue 9, 1 September 2018, Pages 3095–3114

[5] Human brain mapping: A systematic comparison of parcellation methods for the human cerebral cortex, Arslan S, Ktena SI, Makropoulos A, Robinson EC, Rueckert D, Parisot S. Epub 2017 Apr 13.

[6] Arslan, S., Ktena, S.I., Makropoulos, A., Robinson, EC., Rueckert, D., Parisot, S., 2017, Human brain mapping: A systematic comparison of parcellation methods for the human cerebral cortex, NeuroImage, doi: 10.1016/j.neuroimage.2017.04.014

[7] Horn David, and Assaf Gottlieb. "Algorithm for data clustering in pattern recognition problems based on quantum mechanics." Physical review letters 88.1 (2001): 018702

[8] Lior Deutsch and David Horn. The Weight-Shape decomposition of density estimates: A framework for clustering and image analysis algorithms.. https://doi.org/10.1016/j.patcog.2018.03.034, Pattern Recognition, Volume 81, September 2018, Pages 190-199

[9] MRI Segmentation of the Human Brain: Challenges, Methods, and Applications Ivana Despotović, Bart Goossens, and Wilfried Philips Computational and Mathematical Methods in Medicine
Volume 2015, Article ID 450341, http://dx.doi.org/10.1155/2015/450341

[10] Divide and conquer: A defense of functional localizers, Rebecca Saxe ,Matthew Brett ,Nancy Kanwisher. https://doi.org/10.1016/j.neuroimage.2005.12.062

[11] Construction of a 3D probabilistic atlas of human cortical structures, Mubeena Mirza, Vitria Adisetiyo, Cornelius Hojatkashani, Georges Salamon, Katherine L. Narr, Russell A.Poldrack, Robert M.Bildercd, Arthur W. Toga, https://doi.org/10.1016/j.neuroimage.2007.09.031

[12] MR Volume Segmentation of Gray Matter and White Matter Using Manual Thresholding: Dependence on Image Brightness , Gordon J. Harris, Patrick E. Barta, Luon W. Peng, Seong Lee, Paul D. Brettschneider, Amish Shah, Jeffery D. Henderer, Thomas E. Schlaepfer, and Godfrey D. Pearlson , AJNR Am J Neuroradio/15:225-230, Feb 1994

[13] Segmentation of neonatal brain MR images using patch-driven level sets , Li Wang, Feng Shi, Gang Li, Yaozong Gao, Weili Lin, John H. Gilmore, Dinggang Shen. https://doi.org/10.1016/j.neuroimage.2013.08.008

[14] Human brain mapping: A systematic comparison of parcellation methods for the human cerebral cortex, Salim Arslan, Sofia Ira Ktena, Antonios Makropoulos Emma C.Robinson, Daniel Rueckert, Sarah Parisot, https://doi.org/10.1016/j.neuroimage.2017.04.014

[15] Cheng, Yizong. "Mean shift, mode seeking, and clustering." IEEE transactions on pattern analysis and machine intelligence 17.8 (1995): 790-799

[16] Multiplicative intrinsic component optimization (MICO) for MRI bias field estimation and tissue segmentation, Chunming Li, John C. Gore, Christos Davatzikos, https://doi.org/10.1016/j.mri.2014.03.010

[17] Parzen, Emanuel. "On estimation of a probability density function and mode." The annals of mathematical statistics 33.3 (1962): 1065-1076.

[18] Juntu J., Sijbers J., Van Dyck D., Gielen J. (2005) Bias Field Correction for MRI Images. In: Kurzyński M., Puchała E., Woźniak M., żołnierek A. (eds) Computer Recognition Systems. Advances in Soft Computing, vol 30. Springer, Berlin, Heidelberg

[19] MRI brain image segmentation and bias field correction based on fast spatially constrained

kernel clustering approach, Liang Liao, Tusheng, Lin,Bi Li Pattern Recognition Letters Volume

29, Issue 10, 15 July 2008, Pages 1580-1588

[20] "Étude comparative de la distribution florale dans une portion des Alpes et des Jura", Bulletin de la Société Vaudoise des Sciences Naturelles, 37: 547–579. · January 1901

[21] A Data-Driven Approach to Extract Connectivity Structures from Diffusion Tensor Imaging Data, Yu Jin, Joseph F. JaJa , Rong Chen , Edward H. Herskovits, Feb 2018

תקציר

תכונות השכבות השונות המהוות את אזור הקורטקס במוח מגדירות את מבנה החומר האפור והקישוריות בין האזורים השונים במוח ההכרחיים לתפקודו התקין. חקר שכבות אלו עושה שימוש בתמונות דימות מסוג MRI

חקר שכבת הקורטקס מציע חלוקות שונות ומיפוי תמונות דימות אלו לאזורים נפרדים, תהליך המכונה פרסלציית המח. במסגרת עבודה זו פיתחנו מתודולוגיה חדשה לחקר נתוני דימות אלו. המתודולוגיה מתבססת על פונקציית ההסתברות המתקבלת משימוש בחלון פארזן על גבי נתוני הדימות התלת ממדיים, ופירוקה למרכיבי "משקל" ו"צורה" המתארים מאפיינים שונים של פונקציית ההסתברות: ה"צורה" מביאה לידי ביטוי נתונים לוקאליים בעוד ה"משקל" מושפע יותר מההטיה הגלובאלית בנתונים.

ממצאינו מראים כי בחירת נתוני מידע מתוך תמונת הדימות על בסיס אזורים בהם התקבלו ערכים גבוהים של פונקציית ה"צורה" עבור קיטוב מסוג T2 , מתקבלת חלוקה טובה בין מרכיבי החומר האפור מיתר מרכיבי המוח, זאת ללא צורך במידע נוסף על אנטומיית המח. שימוש בטכניקות קליסטור על אותם אזורים הדגימה פרסלצייה יציבה על תמונות דימות של ארבעה קופי מקוק ושלוש חולדות.

בתמונות דימות אשר התקבלו בטכניקת T1 האזורים בהם מתקבלים ערכים גבוהים של פונקציית ה"צורה" כוללים מרכיבי מוח נוספים מלבד החומר האפור. לכן בתמונות אלו אנו מבצעים קליסטור על גבי כל אזורי המוח בתמונות. שיטה זו נבדקה על תמונות דימות של שני בני אדם. השוואה בין ממצאים המתקבלים בין שתי שיטות אלו הראתה התאמה.

שיטות אלו ייחודיות ושימושיות עבור מספר רב של יונקים, ללא צורך בידע מקדים על אנטומיית המוחות.

אוניברסיטת תל-אביב

הפקולטה למדעים מדויקים

ע"ש ריימונד ובברלי סאקלר

פרסלציית דימות מוח באמצעות אנליזת מבנה

חיבור זה הוגש כחלק מהדרישות לקבלת התואר

באוניברסיטת תל-אביב M.Sc. - "מוסמך אוניברסיטה"

בית הספר לפיסיקה ואסטרונומיה

הוגש על ידי

איתי פישר

העבודה הוכנה בהדרכתו של

פרופסור דוד הורן

ופרופסור יניב אסף

ספטמבר 2018